Neptune's carbon monoxide profile and phosphine upper limits from Herschel/SPIRE*: Implications for interior structure and formation

N. A. Teanby[a], P. G. J. Irwin[b], J. I. Moses[c]

[a]*School of Earth Sciences, University of Bristol, Wills Memorial Building, Queens Road, Bristol, BS8 1RJ, U.K.*
[b]*Atmospheric, Oceanic & Planetary Physics, Department of Physics, University of Oxford, Clarendon Laboratory, Parks Road, Oxford, OX1 3PU. UK.*
[c]*Space Science Institute, 4750 Walnut Street, Suite 205, Boulder, CO 80301, USA.*

Abstract

On Neptune, carbon monoxide and phosphine are disequilibrium species, and their abundance profiles can provide insights into interior processes and the external space environment. Here we use Herschel/SPIRE (Spectral and Photometric Imaging REceiver) observations from 14.9–51.5 cm^{-1} to obtain abundances from multiple CO and PH_3 spectral features. For CO, we find that nine CO bands can be simultaneously fitted using a step profile with a 0.22 ppm tropospheric abundance, a 1.03 ppm stratospheric abundance, and a step transition pressure of 0.11 bar near the tropopause. This is in broad agreement with previous studies. However, we also find that the CO spectral features could be fitted, to well within measurement errors, with a profile that contains no tropospheric CO for pressure levels deeper than 0.5 bar,

Email address: n.teanby@bristol.ac.uk (N. A. Teanby)

Herschel is an ESA space observatory with science instruments provided by European-led Principal Investigator consortia and with important participation from NASA.

which is our preferred interpretation. This differs from previous studies that have assumed CO is well mixed throughout the troposphere, which would require an internal CO source to explain and a high O/H enrichment. Our interpretation removes the requirement for extreme interior O/H enrichment in thermochemical models and can finally reconcile D/H and CO measurements. If true, the lack of lower tropospheric CO would imply a decrease in Neptune's interior water content, favouring a silicate-rich instead of an ice-rich interior. This would be consistent with a protoplanetary ice source with a similar D/H ratio to the current solar system comet population. The upper tropospheric and stratospheric CO at pressures less than 0.5 bar could then be entirely externally sourced from a giant impact as suggested by Lellouch et al. (2005). We also derive a 3-σ upper limit for PH_3 of 1.1 ppb at 0.4–0.8 bar. This is the most stringent upper limit to-date and is entirely consistent with predictions from a simple photochemical model.

Keywords: Neptune, Atmosphere, Interior, Composition, sub-millimetre

1. Introduction

Observations of bulk density, gravity, and moment of inertia show that Neptune and Uranus are significantly enriched in heavy elements compared to Jupiter, Saturn, and the solar composition (Hubbard et al., 1995; Podolak et al., 1995; Owen and Encrenaz, 2006; Irwin, 2009; Helled et al., 2011; Nettelmann et al., 2013). Their interiors are expected to contain a significant proportion of ices due to their formation beyond the ice line in the solar nebula, where cold temperatures permitted formation and subsequent ingestion of icy planetesimals. However, the fraction of rock to ice and the nature of

the original planetesimals are currently not well understood and ice-rich and rock-rich interior models are both compatible with the available bulk density, gravity, and moment of inertia observations (Podolak et al., 1995; Helled et al., 2011; Nettelmann et al., 2013). The different formation scenarios and internal structures are consistent with subsets of available spectroscopic observations and important discrepancies remain, particularly when trying to reconcile D/H and O/H measurements (Feuchtgruber et al., 2013). Here we consider two of Neptune's disequilibrium species, carbon monoxide (CO) and phosphine (PH_3), which have the potential to further constrain Neptune's interior composition, formation, and external planetary environment.

CO has been observed on both Uranus (Encrenaz et al., 1996; Cavalié et al., 2014) and Neptune (Marten et al., 1993; Guilloteau et al., 1993; Naylor et al., 1994; Courtin et al., 1996; Lellouch et al., 2005; Marten et al., 2005; Hesman et al., 2007; Lellouch et al., 2010; Fletcher et al., 2010; Luszcz-Cook and de Pater, 2013). On Uranus CO has a stratospheric abundance of 7.1–9.0 ppb (Cavalié et al., 2014) and a 3-σ tropospheric upper limit of 2.1 ppb for pressures around 0.1–0.2 bar (Teanby and Irwin, 2013). On Neptune CO is much more abundant, with recent studies suggesting a step-type profile with 1–3 ppm in the stratosphere and up to 0.5 ppm in the troposphere (summarised in Table 1).

The CO vertical gradient can be used to determine whether its source is mixing from the deep interior or external supply from comets, micrometeorites, or interplanetary dust. However, there is some disagreement in the published abundances (Table 1). The most recent study by Luszcz-Cook and de Pater (2013) found 1–2 ppm in the stratosphere, 0–0.3 ppm in the

troposphere, and a transition pressure of $\sim$0.1 bar (close to the tropopause). This is broadly consistent with Lellouch et al. (2005)'s stratospheric determination of 1 ppm, but lower than their value of 0.5 ppm for the troposphere. Conversely, Hesman et al. (2007)'s tropospheric value is consistent with Lellouch et al. (2005)'s, but has a stratospheric abundance 2–3 times higher. There is also considerable uncertainty on the pressure of the transition in the step profiles used in all three studies. The discrepancy of these results could be partly due to the difficulty of observing CO from ground-based telescopes. The wide CO line wings that probe the troposphere cannot usually be covered with a single observation due to instrument bandwidth limitations. Therefore, either only the central emission core is observed to obtain a stratospheric abundance, or multiple observations with different local oscillator tunings must be stitched together. Such observations require baseline matching, which introduces extra uncertainty as observations must be taken at different times with different sky and instrument background levels. There are also differences in the radiative transfer modelling approaches, in particular the assumed temperature profile. Therefore, new space-based constraints would be extremely valuable.

CO is more thermodynamically stable at the higher temperatures of Neptune's deep atmosphere ($\gtrsim$1000 K, $\gtrsim$5000 bar) and becomes less stable (and much less abundant) in comparison to the thermochemical-equilibrium favoured molecules methane and water in the colder outer region of Neptune's hydrogen-rich atmosphere (Lodders and Fegley, 1994). However, CO destruction reactions have a strong temperature dependence and rapid vertical mixing can advect CO to pressure levels where the CO destruction timescale

is longer than the mixing timescale, effectively quenching the CO destruction and allowing significant CO to mix into the troposphere and stratosphere. On Neptune this quenching is expected to occur at 2000–10000 bars and 850–1100 K depending on the strength of vertical mixing (Luszcz-Cook and de Pater, 2013; Cavalié et al., 2017). Such rapid mixing should result in a uniform CO mixing ratio in the troposphere and stratosphere. For Neptune, plausible estimates of the temperature profile and vertical mixing suggest that O/H must be enriched by at least 280 times relative to solar composition in order to reproduce the observed ∼0.1 ppm CO in the troposphere (Luszcz-Cook and de Pater, 2013; Cavalié et al., 2017). However, such a large enrichment of O/H is not compatible with D/H measurements, which suggest more modest O/H enrichments of ∼50–150 (Feuchtgruber et al., 2013) if Neptune's internal water was sourced from protoplanetary ices with D/H comparable to present day comets. CO has not yet been detected in Uranus' troposphere (Teanby and Irwin, 2013), which could be due to less vigorous mixing.

The excess of CO in both Neptune and Uranus' stratospheres compared to their tropospheres suggests a significant external CO source for both planets (Lellouch et al., 2005; Cavalié et al., 2013). Estimates of the external flux required to explain observed H_2O and CO_2 abundances in Uranus and Neptune's stratosphere were made by Feuchtgruber et al. (1997), suggesting H_2O external fluxes of 0.6–1.6$\times10^5$ molecules cm^{-2}s^{-1} for Uranus and 1.2–150$\times10^5$ molecules cm^{-2}s^{-1} for Neptune. These inferred H_2O influx rates are broadly consistent with those expected from incoming interplanetary dust grains (Poppe, 2016). However, the predicted dust flux for Neptune

is roughly two orders of magnitude too small to explain the very large observed CO abundance in Neptune's stratosphere, even if the oxygen from the dust grains were efficiently converted to CO (see Poppe, 2016; Moses and Poppe, 2017). The large concentration of CO in Neptune's stratosphere led Lellouch et al. (2005) to suggest that the source of Neptune's CO could be a large cometary impact that occurred ∼200 years ago. This hypothesis is supported by the recent detection of CS by Moreno et al. (2017), an impact product that was also detected after the Shoemaker-Levy 9 impact on Jupiter (Moreno et al., 2003). Moreno et al. (2017) suggest a slightly larger 4 km diameter comet impacting ∼1000 years ago.

Further constraints on Neptune's atmosphere can be obtained by studying another disequilibrium species, phosphine (PH_3), which is only stable in the deep atmosphere, but could theoretically be transported to higher atmospheric levels by rapid vertical mixing as on Jupiter and Saturn (Irwin et al., 2004; Fletcher et al., 2009). There is currently considerable uncertainty about Neptune's phosphorous enrichment, but a P/H enrichment of 50 times solar, similar to that inferred for C/H from methane measurements (Baines et al., 1995), is considered reasonable. However, observing PH_3 is challenging as it condenses in Neptune's cold troposphere for pressures less than ∼1 bar. Also, PH_3 is photodissociated by solar UV photons in the upper troposphere of giant planets (Kaye and Strobel, 1984; Moses, 2000), leading to additional depletion in the upper troposphere. This should result in significant PH_3 abundance only for pressures greater than ∼1–2 bar, producing spectral features that are wide due to pressure broadening and with negligible central emission core due to a lack of significant stratospheric abundance.

Nevertheless, an attempt was made to observe the 267 GHz (8.91 cm^{-1}) PH_3 feature by Encrenaz et al. (1996) who determined that a 2 ppm deep PH_3 abundance ($\sim$3x solar P/H) coupled with super-saturation by a factor of 100 above the condensation level was inconsistent with observations from the Caltech Submillimeter Observatory. More recently Moreno et al. (2009) determined a more stringent upper limit of 0.1 times the solar P/H value using the same PH_3 feature observed with the IRAM 30 m telescope, corresponding to an upper troposphere abundance upper limit of $\sim$60 ppb (assuming a solar abundance of P/H=2.81×10^{-7} from Lodders (2010)). Unfortunately, these upper limits are not sufficient to significantly inform photochemical models.

Here we use Herschel/SPIRE data to further constrain Neptune's CO and PH_3 profiles. SPIRE is ideally suited to studying these gases as it covers a wide spectral range containing multiple CO and PH_3 features. This allows the line wings to be measured in a single measurement from a space-based platform with no atmospheric interference. This will permit the most sensitive search of PH_3 to date, more robust constraints on Neptune's CO profile, and insights into Neptune's interior and formation.

2. Observations

Observations were taken with the SPIRE instrument (Griffin et al., 2010; Swinyard et al., 2010) on board the Herschel Space Observatory (Pilbratt et al., 2010). SPIRE is a Fourier transform spectrometer comprising a long-wave spectrometer (SLW) covering wavenumbers 14.9–33.0 cm^{-1} (671–303 μm) and a short-wave spectrometer (SSW) covering 31.9–51.5 cm^{-1} (313–194 μm). The SPIRE spectrometers have hexagonal arrays of circular pixels;

37 pixels for the SLW and 19 pixels for the SSW. The unapodised spectral resolution can be set to low resolution (0.83 cm^{-1}), medium resolution (0.24 cm^{-1}), and high resolution (0.04 cm^{-1}). Herschel's 3.5 m diameter primary mirror combined with the pixel array footprints results in pixel beams with a field-of-view of 17–42", which is large compared to Neptune's ∼2.3" projected diameter, so observations are disc-averaged.

Herschel operated from 2009 until 2013, when it ran out of coolant, and all data are now archived. Uranus was used as the primary flux calibrator for the SPIRE spectrometer (Swinyard et al., 2014), but Neptune was also regularly observed for cross-calibration with the SPIRE photometer observations (Swinyard et al., 2014; Hopwood et al., 2015). The pipeline radiance calibration used a Uranus reference spectrum combined with darks taken on a relatively empty area of sky, which were used to remove the instrument self-emission and characterise the instrument (Swinyard et al., 2010, 2014; Hopwood et al., 2015). We queried the Herschel Science Archive for all science and calibration observations of Neptune taken with SPIRE in high resolution spectrometer mode so that the CO features could be resolved. The Level 2 unapodised calibrated radiances were extracted and convolved with a Hamming function to give an apodised spectral resolution of 0.07373 cm^{-1} (full-width half-maximum) and a sample spacing of 0.01 cm^{-1}. The CO absorption features had widths of ∼0.5 cm^{-1} and the widths of the central emission cores were limited by SPIRE's spectral resolution. The Neptune-centred pixel from each observation was extracted to give a disc-average spectrum and associated pipeline uncertainties. After quality control of the observations to reject spectra with excessive noise or anomalously high/low

radiances, 17 Neptune observations remained with integration times from 823–13762 s. Observations are summarised in Table 2 and Figure 1a and b. Total integration time on Neptune was 32687 s (9 hrs 4 mins 47 s), with all observations taking place during 2009 and 2010.

Prior to further analysis, the 17 individual spectra were combined into a single high signal-to-noise disc-average Neptune spectrum. To account for distance variations and slight calibration differences between observations the weighted average continuum radiances at 20.5–21.5 cm^{-1} and 39.5–40.5 cm^{-1} were calculated and individual spectra were rescaled to match the overall average. This rescaling was required to allow representative variances on the combined spectrum to be calculated, but did not affect the overall mean radiance. All 17 observations were then combined into an average spectrum using the error weighted mean (Bevington and Robinson, 1992). To determine the uncertainties on the combined spectrum we calculated both the error-weighted variance of the 17 spectra and the theoretical error weighed variance based on the pipeline uncertainties of each spectrum; whichever was the largest was used for the uncertainty. Overall uncertainties (standard error) per spectral element were $\sim$0.2 Jy for the SLW and $\sim$0.3 Jy for the SSW. The combined average SLW and SSW spectra are shown in Figure 1c and d. CO absorption and emission features are clearly visible. However, the spectra still contain slight continuum ripples as noted in previous studies (Teanby and Irwin, 2013; Teanby et al., 2013). Removal of these ripples required comparison to a synthetic spectrum and is discussed in the next section.

3. Spectral modelling

To fit the observed SPIRE spectrum and retrieve the composition of CO and PH_3 we used the NEMESIS radiative transfer code (Irwin et al., 2008), which we have previously used to analyse SPIRE spectra for Uranus (Teanby and Irwin, 2013) and Titan (Teanby et al., 2013), in addition to extensive use for analysis of Neptune's near-IR spectra (Irwin et al., 2011, 2014, 2016).

Our Neptune reference atmosphere had a nominal temperature profile based on Voyager 2 radio occultation analysis by Lindal (1992) for pressures greater than 15 mbar, AKARI spectroscopic analysis by Fletcher et al. (2010) for pressures less than 10 mbar, and a linear interpolation (in log pressure) in between. Temperature was gridded onto 71 levels between 0.6 μbar and 6 bar on a regular logarithmic grid. There is some uncertainty regarding Neptune's tropospheric temperature structure, with differences up to 5 K reported in the literature (for example, see discussion in Hesman et al., 2007; Fletcher et al., 2010; Luszcz-Cook and de Pater, 2013). Therefore, we also consider "Hot" and "Cold" profiles, which differ from the nominal profile by $\pm$5 K (Figure 2). For the baseline atmospheric composition we assumed a He/H_2 ratio of 0.15 (by volume) and a volume mixing ratio (VMR) of 0.003 for N_2 (Conrath et al., 1993). The CH_4 volume mixing ratio was set to a deep value of 0.02, followed the saturation pressure vapour curve in the upper troposphere, and had an abundance of 1.15×10^{-3} in the stratosphere (Lellouch et al., 2015). There is some uncertainty on Neptune's deep CH_4 abundance (see discussion in Irwin et al., 2014), but the effect on the SPIRE spectrum is minimal. HCN only has minor spectral features in this range, but we include the abundance profile of Marten et al. (2005) for completeness.

Spectroscopic parameters were the same as those used in Teanby and Irwin (2013).

Synthetic spectra were generated using the correlated-k approximation for computational efficiency (Goody and Yung, 1989; Lacis and Oinas, 1991; Irwin et al., 2008). The k-tables included the Hamming instrument function with a FWHM of 0.07373 cm^{-1}. To simulate the disc-averaged spectrum we used the field-of-view averaging technique detailed in Teanby et al. (2013) with 33 field-of-view points; 20 on Neptune's disc and 13 covering the limb. This accounted for limb brightening and limb darkening effects and was sufficient to reduce the disc-averaged systematic modelling errors, due to emission angle variation across Neptune's disc, to at least five times below the level of the observation uncertainties.

Observed spectra were corrected for minor continuum ripples by comparison with synthetic spectra generated using the reference atmosphere. First, synthetic spectra were created for an atmosphere containing no CO or PH_3. Second, synthetic spectra were created for an atmosphere with the nominal CO profile from Luszcz-Cook and de Pater (2013) and a PH_3 profile with a deep abundance of 1 ppb with the saturation vapour pressure law applied. Third, the difference between spectra with and without CO/PH_3 was used to create a continuum mask where the difference was less than 0.05 Jy, at least a factor of four below the observational uncertainties. Fourth, the mask was applied to the observations to remove spectral regions surrounding the CO and PH_3 line positions, leaving only the continuum points. Fifth, the ratio between masked observation and synthetic was calculated and a smooth cubic b-spline curve fitted using a knot spacing of 3 cm^{-1} for the SLW and

1.5 cm^{-1} for the SSW (Teanby, 2007). These knot spacings were large enough to only remove large scale ripples and did not affect the spectral features. The resulting correction factor f_{corr} is shown in Figure 1e and f and suggests continuum ripples of order $\pm 1\%$. Finally, the fitted smooth correction factor curve was applied to the observations to give the corrected SLW and SSW spectra shown in Figure 1g and h. This procedure was repeated for the nominal, hot, and cold temperature profiles. Note that a CO feature at 15.38 cm^{-1} could not be analysed as it was at the low wavenumber edge of the SLW, so the surrounding continuum level could not be reliably corrected.

To determine the information content of our observed spectra we calculated the contribution functions, defined as the change in irradiance as a function of gas abundance at each pressure level. The contribution functions for each of the CO bands are shown in Figure 3 assuming the SPIRE spectral resolution, the nominal temperature profile, and a 0.1 ppm uniform CO profile. In addition to the SPIRE CO bands, we also calculated the contribution functions for the lower frequency CO (1–0), (2–1), and (3–2) transitions analysed in previous studies. Therefore, for this calculation the temperature profile was extended to 60 bar using the dry adiabatic lapse profile rate from Luszcz-Cook and de Pater (2013) so that contributions from the troposphere for the lowest frequency CO lines were fully determined. Note that contribution functions for the CO (1–0), (2–1), and (3–2) transitions are also calculated at the SPIRE spectral resolution, so are representative of the line wings only, not the central emission cores, which can sound to much lower pressure at high spectral resolution.

Figure 3 shows that there are two main pressure ranges where the SPIRE

spectra have information on CO abundance: ∼1.0–0.1 bar from the wide tropospheric absorption wings of the CO lines, which are most prominent for the SLW observations; and ∼0.001–0.01 bar from the narrow stratospheric emission cores of the CO lines, which are most prominent in the SSW observations. The difference between SLW and SSW CO features is caused by increases in CO line strength and overall atmospheric opacity with increasing wavenumber across the SPIRE range. There is little or no information in the 0.01–0.1 bar region, which explains the large uncertainty in previous determinations of the transition pressure in step-type CO profiles (see e.g. Luszcz-Cook and de Pater, 2013, and Table 1). The SPIRE data are not sensitive to the deep abundance (pressures greater than 1.0 bar), but have excellent coverage of the upper troposphere and stratosphere. The lowest frequency bands, including the CO (1–0), (2–1), and (3–2) transitions analysed in previous studies (Table 1), are sensitive to slightly lower deeper levels than our data. Given the limited bandwidth of previous observations (e.g. Luszcz-Cook and de Pater, 2013) Figure 3 shows the maximum pressure probed is ∼3 bar for the CO (1–0) transition, assuming a 0.1 ppm uniform CO abundance.

The PH_3 contribution functions are shown in Figure 4 assuming a nominal deep abundance of 1 ppb and an abundance following the saturation vapour pressure curve in the troposphere, with a maximum stratospheric abundance set to that at the tropopause cold trap. Saturation vapour pressure temperature dependence was based on a fit to the low temperature vapour pressures in Lide (1995), giving the saturation vapour pressure in bars $P_{\mathrm{SVP}}(T) = \exp(a + b/T + cT)$, where $a = 11.4600$, $b = -1974.44$ K, and

$c = -0.00435846$ K^{-1}. The pressure level where PH_3 condenses is a strong function of temperature, anywhere from 0.1–1 bar, which gives very different contribution functions for the nominal, hot, and cold temperature profiles. However, there is very limited information for pressures greater than 1 bar in these data. There are four PH_3 spectral features covered by SPIRE (centred on 17.81, 26.70, 35.59, and 44.46 cm^{-1}), but the features at 17.81 cm^{-1} (SLW) and 44.46 cm^{-1} (SSW) are the most favourable for a detection as they are well separated from the CO features. The optimal band for searching for PH_3 depends on the temperature profile and abundance profile, with the SLW being optimal for the cold and nominal profiles, and the SSW being optimal for the hot profile.

Spectra were fitted using NEMESIS' iterative non-linear retrieval scheme (Irwin et al., 2008), which adjusts the composition profiles to minimise the misfit between modelled spectrum and observation. Simple parameterised profiles were used for both CO and PH_3, so it was not necessary to impose apriori constraints on the retrieval scheme.

For fitting the CO spectral features we used three profile types: (1) a three parameter simple step profile, defined by a uniform deep abundance v_1, a uniform stratospheric abundance v_2, and a transition pressure p_1; (2) a four parameter gradient profile, defined by a uniform deep abundance v_1, a uniform stratospheric abundance v_2, and two pressures p_1 and p_2, which defined a transitional linear gradient region (in log pressure-abundance) from v_1 to v_2; and (3) a four parameter external gradient profile with zero deep abundance for pressures greater than p_1, a linear transition region (in log pressure-abundance) defined by two pressure-abundance pairs (p_1, v_1) and

307 (p_2, v_2), and uniform abundance v_2 at pressures less than p_2. The step profile
308 (1) has been used extensively in the literature to represent a combination
309 of internal and external sources. The gradient profile (2) expands on the
310 step profile slightly by allowing a finite mixing region. The external gradient
311 profile (3) represents the case where there is no significant internal CO source
312 and all tropospheric CO is mixed from above.

313 For PH_3, we used a single parameter profile based on a uniform deep
314 abundance modified by the saturation vapour pressure and with the strato-
315 spheric abundance set to that at the troposphere cold trap.

316 4. Results

317 All nine CO spectral features were fitted simultaneously for each of the
318 three CO profile types and assuming a nominal, hot, or cold temperature
319 profile. Table 3 summarises the fit parameters for each case. The quality of
320 each fit was assessed using the χ^2 statistic:

$$\chi^2 = \sum_{i=1}^{N} \left[\frac{I_{\rm obs}(\nu_i) - I_{\rm fit}(\nu_i)}{\sigma(\nu_i)} \right]^2 \quad (1)$$

321 where ν_i is the wavenumber, $I_{\rm obs}(\nu_i)$ is the measured spectral irradiance,
322 $I_{\rm fit}(\nu_i)$ is the best fitting synthetic spectrum, $\sigma(\nu_i)$ is the observational error,
323 and N is the number of points in the spectrum. The reduced χ^2 defined by
324 χ^2/N should be $\sim$1 if the synthetic spectrum fits the data within error.

325 The nominal temperature profile combined with the step CO profile had
326 the lowest χ^2/N (0.63), which we consider our best fitting model. Figure 5
327 shows the best fit to the nine CO features covered by SPIRE, assuming the
328 nominal temperature profile and using the step profile with deep abundance

of 0.22 ppm, a stratospheric abundance of 1.03 ppm and a transition pressure of 0.11 bar. The reduced χ^2 is less than 1, suggesting the data are well fitted by this profile. In fact, the χ^2/N only exceeds 1 for the hot external gradient profile, but for all other cases the fits can be considered adequate. While the nominal temperature step profile technically provides the best fit to the data, it cannot be statistically distinguished from the other temperature / CO profile cases. Therefore, a wide range of profiles can fit these data, including those with no internal CO source. The fitted profiles are shown in Figure 6a and can all be considered plausible. The range of abundances obtained were 0–0.36 ppm for the deep volume mixing ratio and 0.80–1.55 ppm for the stratospheric volume mixing ratio. The transition pressure range is not well determined by these data, but falls between 0.11–0.75 bar.

None of the four phosphine spectral features covered by SPIRE were visible in the data. Therefore, we determined upper limits using a modified χ^2, $\chi^2_r(v)$:

$$\chi^2_r(v) \quad = \quad \frac{\Delta\nu_{\rm obs}}{\Delta\nu_{\rm res}} \sum_{i=1}^{N} \left[\frac{I_{\rm obs}(\nu_i) - I_{\rm fit}(\nu_i, v)}{\sigma(\nu_i)} \right]^2 \qquad (2)$$

where $\Delta\nu_{\rm obs}$ is the observation wavenumber spacing (0.01 cm^{-1}), $\Delta\nu_{\rm res}$ is the observation spectral resolution (0.07373 cm^{-1}), and v is the deep PH_3 volume mixing ratio. The factor $\Delta\nu_{\rm obs}/\Delta\nu_{\rm res}$ accounts for the spectral oversampling. The PH_3 profile is defined by one parameter so the 3-σ upper limit is defined as the abundance which increases χ^2_r by +9 (Press et al., 1992).

Figure 7 shows the variation of $\Delta\chi^2_r = \chi^2_r(v) - \chi^2_r(0)$ as a function of PH_3 abundance for the nominal, hot, and cold temperature profiles, along with the observed spectra and 3-σ upper limit synthetics. The SLW 17.81 cm^{-1} and

SSW 44.46 cm^{-1} bands were considered independently and the best upper limits for each assumed temperature profile are summarised in Table 4. The PH_3 upper limit for the nominal temperature profile was 1.10 ppb. Figure 6b shows the upper limits and indicates the pressure range of the information content.

5. Discussion

5.1. CO profile

Our retrieved CO abundances are broadly consistent with previous results and agree with those presented by Luszcz-Cook and de Pater (2013) (Table 1). The step profile results provide the most direct comparison as this profile was also used in the previous studies (Lellouch et al., 2005; Hesman et al., 2007; Lellouch et al., 2010; Luszcz-Cook and de Pater, 2013). Our preferred deep abundance of 0.21–0.24 is most consistent with Luszcz-Cook and de Pater (2013) and Hesman et al. (2007), whereas our stratospheric abundance of 0.80–1.41 is most consistent with Luszcz-Cook and de Pater (2013) and Lellouch et al. (2005). The advantage of our CO profiles over previous studies is that the SPIRE data cover a much larger spectral range, allowing the wide CO line wings and narrow emission cores to be measured at the same time. We also fit nine CO bands simultaneously, providing an extra consistency check compared to previous studies, which fitted between one and three bands (Table 1). However, the SPIRE observations are at relatively low spectral resolution compared to previous microwave studies, so cannot fully resolve the emission cores, resulting in reduced sensitivity

at very low pressures (<0.1 mbar). Our observations are also at higher frequency compared to previous studies and do not sound below 1 bar.

One key feature of the SPIRE observations is they do not require significant CO for pressures greater than 0.5 bar, and CO is only required in the upper troposphere (0.1–0.5 bar) to adequately fit the data. This was also apparent in some of the solutions found by Luszcz-Cook and de Pater (2013), which included the J=1-0 line at 115.271 GHz, which has contribution functions that extend slightly deeper than our data (to ∼3 bar assuming a uniform CO profile (Figure 3)).

Therefore, by combining our results with those of Luszcz-Cook and de Pater (2013) we infer that while some CO is required in the upper troposphere (0.1–0.5 bar) to fit the observations, it is not a requirement to have significant amounts at deeper pressures. This has important implications for the formation and composition of Neptune's deep atmosphere and could resolve some of the apparent discrepancies between CO and D/H measurements.

5.2. Neptune's formation and internal structure

D/H in Neptune's atmosphere has been measured to be $4.1\pm0.4\times10^{-4}$ from Herschel/PACS observations (Feuchtgruber et al., 2013). When this is combined with water-rich interior models fitted to mass, moment of inertia, and gravitational coefficients from the Voyager 2 flyby (Hubbard et al., 1995; Podolak et al., 1995; Helled et al., 2011; Nettelmann et al., 2013), this value of D/H suggests the icy planetesimals that formed Neptune had D/H ratios of $5.1–7.7\times10^{-5}$. This is ∼2–3 times less enriched that any known source material in the present day solar system, with comets having a D/H ratio of $\sim1.5–3.0\times10^{-4}$ (Hartogh et al., 2011).

One potential solution proposed by Feuchtgruber et al. (2013) is to increase the silicate content of the pre-Neptune planetesimals to 68–86% rock an 14–32% ice, i.e. similar to the estimated bulk rock fraction of Pluto (Simonelli and Reynolds, 1989). This would give Neptune a more rock-rich interior compared to more conventional water-rich internal models (Hubbard et al., 1995) and would allow water to be sourced from ices with D/H in the range of current comets ($1.5–3.0\times10^{-4}$). The reduced ice content then puts the O/H enrichment contribution due to Neptune's water ice content to be 50–150 times solar (Feuchtgruber et al., 2013). This solution is appealing as the resulting inferred rock content is also consistent with predictions from the Solar Composition Icy Planetesimals (SCIPs) model of planet formation (Owen and Encrenaz, 2006) and simple formation models using either comet-like or clathrate-hydrate planetesimals (Ali-Dib and Lakhlani, 2018). The inferred O/H enrichment is also comparable with C/H enrichment, which is estimated at ∼50 times solar based on methane measurements by Baines et al. (1995).

However, a problem arises when comparing this potential formation and interior model with thermochemical schemes for CO, which require highly enriched O/H ratios of 280–650 times solar to allow sufficient mixing of CO into the troposphere to explain the previously derived ∼0.1 ppm abundances (Lodders and Fegley, 1994; Luszcz-Cook and de Pater, 2013; Cavalié et al., 2017). For example, Cavalié et al. (2017) used a 1-D thermochemical kinetics and transport model to predict the CO mixing ratio profile on Neptune for different assumptions about the deep O/H abundance. They found that a deep atmospheric O/H ratio of ∼540 times the solar ratio was required to

explain a tropospheric CO mixing ratio of 0.2 ppm, if they assumed the fast CO $\rightarrow$ CH_4 chemical conversion scheme described in Venot et al. (2012). However, as is discussed by Visscher et al. (2010), Moses et al. (2011), and Moses (2014), the adoption of a very large rate coefficient for the reaction H + CH_3OH $\rightarrow$ CH_3 + H_2O in the Venot et al. (2012) scheme likely leads to an overestimate in the required deep O/H abundance on the giant planets. Using the Moses et al. (2011) rate coefficient for this reaction, Cavalié et al. (2017) derive a deep O/H ratio of $\sim$280 for Neptune in order to produce an upper tropospheric CO mixing ratio of 0.2 ppm. This O/H value is still too large to be compatible with the D/H ratio, as discussed above.

One potential solution to reconcile the CO and D/H measurements is to form Neptune (and Uranus) on the CO ice line (Ali-Dib et al., 2014). In this model CO pebbles are concentrated near the ice line due a combination of rapid outward diffusion of CO gas and slow inward migration of pebbles due to gas drag. If Neptune forms close to this ice line then the pre-Neptune planetesimals are largely composed of CO instead of H_2O, resulting in the bulk of Neptune's water originating from transformation of CO into H_2O in the planets interior. This would then be compatible with a higher more comet-like D/H ratio for the water-rich planetesimals contributing to Neptune's formation.

We propose an alternative and perhaps simpler solution – that there is in fact no significant tropospheric CO for pressures greater than $\sim$0.5 bar – and that the majority of Neptune's observable CO is externally sourced. This hypothesis would be consistent with our observations and those of Luszcz-Cook and de Pater (2013) and relaxes the requirement for extreme O/H enrich-

ment in the deep interior. A requirement of this scenario is that the eddy mixing coefficient K in the upper troposphere is reduced so that sufficient CO from a comet impact can be maintained in the 0.1–0.5 bar pressure range to fit the observations. The current estimate of K=10^8 cm^2s^{-1} in the deep troposphere is based on mixing length theory and internal heat flux (Moses, 1992; Moses et al., 1992) and in the absence of other constraints is generally applied to the whole troposphere. However, this heat flux is effectively emitted from the radiative convective boundary, which is likely to be somewhat below the tropopause. Comparing Neptune's observed brightness temperature of 60 K near the ∼100 μm peak of its infrared emission (Burgdorf et al., 2003) to the temperature profiles in Figure 2 suggests a pressure level of ∼0.5 bar for this emission level. The lapse rate is also somewhat reduced in the upper troposphere region, suggesting a more stable atmosphere close to the tropopause than deeper in the atmosphere. Therefore, a reduced K in the 0.1–0.5 bar range is plausible, and is also in line with requirements from recent photochemical modelling (Moses et al., 2018). In this case the external CO source would also still be compatible with the giant comet impact proposed by (Lellouch et al., 2005) and supported by (Moreno et al., 2017). The silicate-rich Neptune suggested by Feuchtgruber et al. (2013) would then be more compatible with the available observations than a water-rich Neptune.

5.3. Phosphorous chemistry

Our PH_3 upper limits of 0.192–5.52 ppb for 0.1–1.2 bar are one to two orders of magnitude more stringent that previous determinations (Encrenaz et al., 1996; Moreno et al., 2009) and show that PH_3 can be considered negligible in the upper troposphere and stratosphere. If the tropospheric

PH_3 profile is determined entirely by condensation of a deep abundance then our upper limits are significantly sub-solar; corresponding to enrichments of 3.93×10^{-4}–1.13×10^{-2} times the Lodders (2010) solar values (Table 4). This is at least three orders of magnitude below the expected ∼50 times enrichment expected from methane measurements and formation models, so suggests other loss processes must be active.

To test whether the lack of PH_3 in this region of Neptune's atmosphere has a photochemical origin, we developed a simple, global-average, one-dimensional model for tropospheric and stratospheric chemistry on Neptune that includes PH_3 photochemistry, using the Caltech/JPL KINETICS code (Allen et al., 1981; Yung et al., 1984). The model inputs are similar to those discussed by Moses and Poppe (2017), but we add nitrogen and phosphorous species and reactions based on the Jupiter and Saturn studies described in Kaye and Strobel (1983b), Kaye and Strobel (1983a), Kaye and Strobel (1984), Visscher et al. (2009), Moses et al. (2010), and Fletcher et al. (2018). We assume that the PH_3 mixing ratio at the model lower boundary (8 bar) is either 2.0×10^{-5} or 4.6×10^{-5} (∼30x or ∼70x solar, based on the protosolar abundances of Lodders et al. (2009)). The eddy diffusion coefficient profile adopted in the model is shown in Fig. 4 of Moses et al. (2018), and is based on the hydrocarbon photochemical modelling discussed in Moses et al. (2005). Although the eddy diffusion coefficients increase with increasing altitude in the stratosphere of Neptune, Moses et al. (2005, 2018) find that the eddy diffusion coefficient must be small (assumed 400 cm^2s^{-1}) in the upper troposphere and/or lower stratosphere of Neptune in order for the large observed C_2H_6 abundance to be reproduced. This is consistent with the qualitative

radiative arguments given in Section 5.2. Our models include absorption of solar radiation by atmospheric gases and multiple Rayleigh scattering by gaseous H_2, He, and CH_4, but we do not consider aerosol extinction.

The results from this photochemical model indicate that PH_3 should be confined to pressures greater than ∼1 bar on Neptune (Figure 6b), consistent with our derived PH_3 upper limits. Phosphine is photolysed by solar ultraviolet photons with wavelengths less than 230 nm. The main products are PH_2 + H. The resulting atomic H can also react with PH_3 to produce PH_2 + H_2, and two PH_2 radicals can combine to form P_2H_4, which then condenses (Ferris and Benson, 1981; Kaye and Strobel, 1984). In this way, the PH_3 is relatively efficiently converted to diphosphine and other phosphorus-bearing aerosols in Neptune's troposphere. Solar photons with wavelengths less than 230 nm do not penetrate past the ∼2–3 bar level in Neptune's troposphere, but multiple Rayleigh scattering allows significant photolysis of PH_3 in the ∼0.5–2.5 bar region, limiting the vertical extent of PH_3. The low eddy diffusion coefficient in this region prevents PH_3 from being transported up faster than it can be destroyed by photolysis. This result could change if the eddy diffusion coefficient in the upper troposphere were greater than we have assumed or if aerosols (not included in the model) shield the PH_3 from photolysis. Our strong upper limits on the PH_3 mixing ratio in the 0.5–1 bar region will allow for useful constraints on the strength of atmospheric mixing in the upper troposphere of Neptune using future models that include aerosol extinction.

6. Conclusion

We used all available Herschel/SPIRE observations to constrain Neptune's CO and PH_3 abundances. A simultaneous fit of all nine CO bands was possible using conventional step profiles, gradient profiles, and profiles with zero deep abundance for pressures greater than 0.5 bar. The fitting of multiple CO bands simultaneously improved the robustness of our abundance results. Our abundances ranged from 0.80–1.55 ppm in the stratosphere (<0.1 bar) and 0.21–0.36 in the upper troposphere (1.0–0.1 bar), in broad agreement with previous studies.

Importantly, the Herschel/SPIRE data to not require tropospheric CO to exist at pressure levels deeper than 0.5 bar. This is also true of previous observations of longer wavelength CO lines by Luszcz-Cook and de Pater (2013) that probe slightly deeper ($\sim$3 bar for the 115 GHz line depending on profile assumptions). Therefore, both our observations and those previously published are not very sensitive to the deep CO abundance, meaning that we cannot confirm or deny the presence of CO for pressures deeper than 1 bar. Caution must then be used in assuming that abundances measured in the upper troposphere are representative of the deep interior.

We suggest that the $\sim$0.1–0.2 ppm deep tropospheric abundances previously reported could in fact be a result of extrapolating an idealised profile to pressures where the data do not constrain the CO abundance. If this is the case then extreme O/H enrichments would no longer be required in thermochemical interior models to explain a CO abundance throughout the troposphere, which allows the CO abundance profile and D/H measurements to be reconciled. This means that current solar system water reservoirs become

a plausible water source, especially if the rock content of Neptune's interior can be increased to dilute the high D/H ratio in these sources. The bulk of Neptune's stratospheric and tropospheric CO can then be considered entirely externally sourced from a large cometary impact within the past few hundred years. We propose that a rock-rich Neptune as proposed by Feuchtgruber et al. (2013) is more compatible with the current geophysical/spectroscopic observations and possible formation scenarios.

PH_3 upper limits are sensitive to the temperature profile assumptions, but fall in the range 0.192–5.52 ppb for the 0.1–1.2 bar pressure range, with a nominal value of 1.10 ppb. This corresponds to 3.93×10^{-4}–1.13×10^{-2} times the solar value, which requires loss processes other than condensation to explain. This is most likely due to photochemistry and the derived upper limits are consistent with our simple photochemical modelling, which predicts negligible PH_3 in this pressure region.

7. Acknowledgements

This work was funded by the UK Science and Technology Facilities Council. SPIRE has been developed by a consortium of institutes led by Cardiff University (UK) and including Univ. Lethbridge (Canada); NAOC (China); CEA, LAM (France); IFSI, Univ. Padua (Italy); IAC (Spain); Stockholm Observatory (Sweden); Imperial College London, RAL, UCL-MSSL, UKATC, Univ. Sussex (UK); and Caltech, JPL, NHSC, Univ. Colorado (USA). This development has been supported by national funding agencies: CSA (Canada); NAOC (China); CEA, CNES, CNRS (France); ASI (Italy); MCINN (Spain); SNSB (Sweden); STFC, UKSA (UK); and NASA (USA).

References

Ali-Dib, M., Lakhlani, G., 2018. What is Neptune's D/H ratio really telling us about its water abundance? Mon. Not. R. Astron. Soc. 476, 1169–1173.

Ali-Dib, M., Mousis, O., Petit, J.-M., Lunine, J. I., 2014. The Measured Compositions of Uranus and Neptune from their Formation on the CO Ice Line. Astrophys. J. 793, 1–7.

Allen, M., Yung, Y. L., Waters, J. W., 1981. Vertical transport and photochemistry in the terrestrial mesosphere and lower thermosphere (50-120 km). J. Geophys. Res. 86, 3617–3627.

Baines, K. H., Mickelson, M. E., Larson, L. E., Ferguson, D. W., 1995. The abundances of methane and ortho/para hydrogen on Uranus and Neptune: Implications of New Laboratory 4-0 H2 quadrupole line parameters. Icarus 114, 328–340.

Bevington, P. R., Robinson, D. K., 1992. Data reduction and error analysis for the physical sciences, 2nd Edition. WBC/McGraw-Hill, New York.

Burgdorf, M., Orton, G. S., Davis, G. R., Sidher, S. D., Feuchtgruber, H., Griffin, M. J., Swinyard, B. M., 2003. Neptune's far-infrared spectrum from the ISO long-wavelength and short-wavelength spectrometers. Icarus 164, 244–253.

Cavalié, T., Feuchtgruber, H., Lellouch, E., de Val-Borro, M., Jarchow, C., Moreno, R., Hartogh, P., Orton, G., Greathouse, T. K., Billebaud, F.,

593 Dobrijevic, M., Lara, L. M., González, A., Sagawa, H., 2013. Spatial dis-
594 tribution of water in the stratosphere of Jupiter from Herschel HIFI and
595 PACS observations. Astron. Astrophys. 553, A21.

596 Cavalié, T., Moreno, R., Lellouch, E., Hartogh, P., Venot, O., Orton, G. S.,
597 Jarchow, C., Encrenaz, T., Selsis, F., Hersant, F., Fletcher, L. N., 2014.
598 The first submillimeter observation of CO in the stratosphere of Uranus.
599 Astron. Astrophys. 562, A33.

600 Cavalié, T., Venot, O., Selsis, F., Hersant, F., Hartogh, P., Leconte, J.,
601 2017. Thermochemistry and vertical mixing in the tropospheres of Uranus
602 and Neptune: How convection inhibition can affect the derivation of deep
603 oxygen abundances. Icarus 291, 1–16.

604 Conrath, B. J., Gautier, D., Owen, T. C., Samuelson, R. E., 1993. Constraints
605 on N_2 in Neptune's atmosphere from Voyager measurements. Icarus 101,
606 168–171.

607 Courtin, R., Gautier, D., Strobel, D., 1996. The CO Abundance on Neptune
608 from HST Observations. Icarus 123, 37–55.

609 Encrenaz, T., Serabyn, E., Weisstein, E. W., 1996. Millimeter Spectroscopy
610 of Uranus and Neptune: Constraints on CO and PH_3 Tropospheric Abun-
611 dances. Icarus 124, 616–624.

612 Ferris, J., Benson, R., 1981. An investigation of the mechanism of phosphine
613 photolysis. J. Am. Chem. Soc. 103 (8), 1922–1927.

614 Feuchtgruber, H., Lellouch, E., de Graauw, T., Bézard, B., Encrenaz, T.,

615 Griffin, M., 1997. External supply of oxygen to the atmospheres of the
616 giant planets. Nature 389, 159–162.

617 Feuchtgruber, H., Lellouch, E., Orton, G., de Graauw, T., Vandenbussche,
618 B., Swinyard, B., Moreno, R., Jarchow, C., Billebaud, F., Cavalié, T.,
619 Sidher, S., Hartogh, P., 2013. The D/H ratio in the atmospheres of Uranus
620 and Neptune from Herschel-PACS observations. Astron. Astrophys. 551,
621 1–9.

622 Fletcher, L. N., Drossart, P., Burgdorf, M., Orton, G. S., Encrenaz, T., 2010.
623 Neptune's atmospheric composition from AKARI infrared spectroscopy.
624 Astron. Astrophys. 514, A17.

625 Fletcher, L. N., Greathouse, T. K., Moses, J. I., Guerlet, S., West, R. A.,
626 2018. Saturn's Seasonally Changing Atmosphere: Thermal Structure,
627 Composition and Aerosols. In: Baines, K., Flasar, M., Krupp, N., Stallard,
628 T. (Eds.), Saturn in the 21st Century. Cambridge Univ. Press, Cambridge,
629 pp. 1–34.

630 Fletcher, L. N., Orton, G. S., Teanby, N. A., Irwin, P. G. J., 2009. Phosphine
631 on Jupiter and Saturn from Cassini/CIRS. Icarus 202, 543–564.

632 Goody, R. M., Yung, Y. L., 1989. Atmospheric Radiation: Theoretical Basis,
633 2nd Edition. Oxford University Press, Oxford.

634 Griffin, M. J., and 178 co-authors, 2010. The Herschel-SPIRE instrument
635 and its in-flight performance. Astron. Astrophys. 518, L3.

636 Guilloteau, S., Dutrey, A., Marten, A., Gautier, D., 1993. CO in the tropo-
637 sphere of Neptune: Detection of the J = 1-0 line in absorption. Astron.
638 Astrophys. 279, 661–667.

639 Hartogh, P., Lis, D. C., Bockelée-Morvan, D., de Val-Borro, M., Biver, N.,
640 Küppers, M., Emprechtinger, M., Bergin, E. A., Crovisier, J., Rengel, M.,
641 Moreno, R., Szutowicz, S., Blake, G. A., 2011. Ocean-like water in the
642 Jupiter-family comet 103P/Hartley 2. Nature 478, 218–220.

643 Helled, R., Anderson, J. D., Podolak, M., Schubert, G., 2011. Interior Models
644 of Uranus and Neptune. Astrophys. J. 726, 1–7.

645 Hesman, B. E., Davis, G. R., Matthews, H. E., Orton, G. S., 2007. The
646 abundance profile of CO in Neptune's atmosphere. Icarus 186, 342–353.

647 Hopwood, R., Polehampton, E. T., Valtchanov, I., Swinyard, B. M., Ful-
648 ton, T., Lu, N., Marchili, N., van der Wiel, M. H. D., Benielli, D., Imhof,
649 P., Baluteau, J.-P., Pearson, C., Clements, D. L., Griffin, M. J., Lim,
650 T. L., Makiwa, G., Naylor, D. A., Noble, G., Puga, E., Spencer, L. D.,
651 2015. Systematic characterization of the Herschel SPIRE Fourier Trans-
652 form Spectrometer. Mon. Not. R. Astron. Soc. 449, 2274–2303.

653 Hubbard, W. B., Podolak, M., Stevenson, D. J., 1995. The interior of Nep-
654 tune. In: Cruikshank, D. P., Matthews, M. S., Schumann, A. M. (Eds.),
655 Neptune and Triton. Space Science Series. University of Arizona Press,
656 Tucson, pp. 109–138.

657 Irwin, P., Teanby, N., de Kok, R., Fletcher, L., Howett, C., Tsang, C., Wil-
658 son, C., Calcutt, S., Nixon, C., Parrish, P., 2008. The NEMESIS planetary

atmosphere radiative transfer and retrieval tool. J. Quant. Spectro. Rad. Trans. 109, 1136–1150.

Irwin, P. G. J., 2009. Giant planets of our solar system: atmospheres, composition, and structure, 2nd Edition. Springer-Praxis, Chichester UK.

Irwin, P. G. J., Fletcher, L. N., Tice, D., Owen, S. J., Orton, G. S., Teanby, N. A., Davis, G. R., 2016. Time variability of Neptune's horizontal and vertical cloud structure revealed by VLT/SINFONI and Gemini/NIFS from 2009 to 2013. Icarus 271, 418–437.

Irwin, P. G. J., Lellouch, E., de Bergh, C., Courtin, R., Bézard, B., Fletcher, L. N., Orton, G. S., Teanby, N. A., Calcutt, S. B., Tice, D., Hurley, J., Davis, G. R., 2014. Line-by-line analysis of Neptune's near-IR spectrum observed with Gemini/NIFS and VLT/CRIRES. Icarus 227, 37–48.

Irwin, P. G. J., Parrish, P., Fouchet, T., Calcutt, S. B., Taylor, F. W., Simon-Miller, A. A., Nixon, C. A., 2004. Retrievals of jovian tropospheric phosphine from Cassini/CIRS. Icarus 172, 37–49.

Irwin, P. G. J., Teanby, N. A., Davis, G. R., Fletcher, L. N., Orton, G. S., Tice, D., Kyffin, A., 2011. Uranus' cloud structure and seasonal variability from Gemini-North and UKIRT observations. Icarus 212, 339–350.

Kaye, J. A., Strobel, D. F., 1983a. Formation and photochemistry of methylamine in Jupiter's atmosphere. Icarus 55, 399–419.

Kaye, J. A., Strobel, D. F., 1983b. HCN formation on Jupiter - The coupled photochemistry of ammonia and Acetylene. Icarus 54, 417–433.

Kaye, J. A., Strobel, D. F., Sep. 1984. Phosphine photochemistry in the atmosphere of Saturn. Icarus 59, 314–335.

Lacis, A. A., Oinas, V., 1991. A description of the correlated k distribution method for modeling nongray gaseous absorption, thermal emission, and multiple-scattering in vertically inhomogeneous atmospheres. J. Geophys. Res. 96 (D5), 9027–9063.

Lellouch, E., Hartogh, P., Feuchtgruber, H., Vandenbussche, B., de Graauw, T., Moreno, R., Jarchow, C., Cavalié, T., Orton, G., Banaszkiewicz, M., Blecka, M. I., Bockelée-Morvan, D., Crovisier, J., Encrenaz, T., Fulton, T., Küppers, M., Lara, L. M., Lis, D. C., Medvedev, A. S., Rengel, M., Sagawa, H., Swinyard, B., Szutowicz, S., Bensch, F., Bergin, E., Billebaud, F., Biver, N., Blake, G. A., Blommaert, J. A. D. L., Cernicharo, J., Courtin, R., Davis, G. R., Decin, L., Encrenaz, P., Gonzalez, A., Jehin, E., Kidger, M., Naylor, D., Portyankina, G., Schieder, R., Sidher, S., Thomas, N., de Val-Borro, M., Verdugo, E., Waelkens, C., Walker, H., Aarts, H., Comito, C., Kawamura, J. H., Maestrini, A., Peacocke, T., Teipen, R., Tils, T., Wildeman, K., Jul. 2010. First results of Herschel-PACS observations of Neptune. Astron. Astrophys. 518, L152.

Lellouch, E., Moreno, R., Orton, G. S., Feuchtgruber, H., Cavalié, T., Moses, J. I., Hartogh, P., Jarchow, C., Sagawa, H., Jul. 2015. New constraints on the CH_4 vertical profile in Uranus and Neptune from Herschel observations. Astron. Astrophys., A121.

Lellouch, E., Moreno, R., Paubert, G., 2005. A dual origin for Neptune's carbon monoxide? Astron. Astrophys. 430, L37–L40.

Lide, D. R. (Ed.), 1995. CRC handbook of chemistry and physics, 76th Edition. CRC Press, Inc., Boca Raton.

Lindal, G. F., 1992. The atmosphere of Neptune - an analysis of radio occultation data acquired with Voyager 2. Astron. J. 103, 967–982.

Lodders, K., 2010. Solar system abundances of the elements. In: Goswami, A., Reddy, B. E. (Eds.), Principles and Perspectives in Cosmochemistry. Springer Berlin Heidelberg, Berlin, Heidelberg, pp. 379–417.

Lodders, K., Fegley, Jr., B., 1994. The origin of carbon monoxide in Neptunes's atmosphere. Icarus 112, 368–375.

Lodders, K., Palme, H., Gail, H.-P., 2009. Abundances of the Elements in the Solar System. Landolt Börnstein.

Luszcz-Cook, S. H., de Pater, I., 2013. Constraining the origins of Neptune's carbon monoxide abundance with CARMA millimeter-wave observations. Icarus 222, 379–400.

Marten, A., Gautier, D., Owen, T., Sanders, D. B., Matthews, H. E., Atreya, S. K., Tilanus, R. P. J., Deane, J. R., 1993. First observations of CO and HCN on Neptune and Uranus at millimeter wavelengths and the implications for atmospheric chemistry. Astrophys. J. 406, 285–297.

Marten, A., Matthews, H. E., Owen, T., Moreno, R., Hidayat, T., Biraud, Y., 2005. Improved constraints on Neptune's atmosphere from submillimetre-wavelength observations. Astron. Astrophys. 429, 1097–1105.

Moreno, R., Lellouch, E., Cavalié, T., Moullet, A., 2017. Detection of CS in Neptune's atmosphere from ALMA observations. Astron. Astrophys. 608, L5.

Moreno, R., Marten, A., Lellouch, E., 2009. Search for PH_3 in the Atmospheres of Uranus and Neptune at Millimeter Wavelength. In: AAS/Division for Planetary Sciences Meeting Abstracts #41. Vol. 41 of AAS/Division for Planetary Sciences Meeting Abstracts. p. 28.02.

Moreno, R., Marten, A., Matthews, H. E., Biraud, Y., 2003. Long-term evolution of CO, CS and HCN in Jupiter after the impacts of comet Shoemaker-Levy 9. Plan. & Space Sci. 51, 591–611.

Moses, J., 2000. Photochemistry in Giant-Planet Atmospheres. In: Griffith, C. A., Marley, M. S. (Eds.), From Giant Planets to Cool Stars. Vol. 212 of Astronomical Society of the Pacific Conference Series. pp. 196–206.

Moses, J. I., 1992. Meteoroid ablation in Neptune's atmosphere. Icarus 99, 368–383.

Moses, J. I., 2014. Chemical kinetics on extrasolar planets. Phil. Trans. R. Soc. Lond. A 372, 20130073.

Moses, J. I., Allen, M., Yung, Y. L., 1992. Hydrocarbon nucleation and aerosol formation in Neptune's atmosphere. Icarus 99, 318–346.

Moses, J. I., Fletcher, L. N., Greathouse, T. K., Orton, G. S., Hue, V., 2018. Seasonal stratospheric photochemistry on Uranus and Neptune. Icarus 307, 124–145.

748 Moses, J. I., Fouchet, T., Bézard, B., Gladstone, G. R., Lellouch, E., Feucht-
749 gruber, H., Aug. 2005. Photochemistry and diffusion in Jupiter's strato-
750 sphere: Constraints from ISO observations and comparisons with other
751 giant planets. J. Geophys. Res. 110, 8001.

752 Moses, J. I., Poppe, A. R., 2017. Dust ablation on the giant planets: Conse-
753 quences for stratospheric photochemistry. Icarus 297, 33–58.

754 Moses, J. I., Visscher, C., Fortney, J. J., Showman, A. P., Lewis, N. K.,
755 Griffith, C. A., Klippenstein, S. J., Shabram, M., Friedson, A. J., Marley,
756 M. S., Freedman, R. S., Aug. 2011. Disequilibrium Carbon, Oxygen, and
757 Nitrogen Chemistry in the Atmospheres of HD 189733b and HD 209458b.
758 Astrophys. J., 15.

759 Moses, J. I., Visscher, C., Keane, T. C., Sperier, A., 2010. On the abundance
760 of non-cometary HCN on Jupiter. Faraday Discussions 147, 103–136.

761 Naylor, D. A., Davis, G. R., Griffin, M. J., Clark, T. A., Gautier, D., Marten,
762 A., 1994. Broad-band spectrscopic detection of the CO J=3-2 tropospheric
763 absorption in the atmosphere of Neptune. Astron. Astrophys. 291, L51–
764 L53.

765 Nettelmann, N., Helled, R., Fortney, J. J., Redmer, R., 2013. New indication
766 for a dichotomy in the interior structure of Uranus and Neptune from the
767 application of modified shape and rotation data. Plan. & Space Sci. 77,
768 143–151.

769 Owen, T., Encrenaz, T., 2006. Compositional constraints on giant planet
770 formation. Plan. & Space Sci. 54, 1188–1196.

771 Pilbratt, G. L., Riedinger, J. R., Passvogel, T., Crone, G., Doyle, D., Gageur,
772 U., Heras, A. M., Jewell, C., Metcalfe, L., Ott, S., Schmidt, M., 2010. Her-
773 schel Space Observatory. An ESA facility for far-infrared and submillimetre
774 astronomy. Astron. Astrophys. 518, L1.

775 Podolak, M., Weizman, A., Marley, M., 1995. Comparative models of Uranus
776 and Neptune. Plan. & Space Sci. 43, 1517–1522.

777 Poppe, A. R., 2016. An improved model for interplanetary dust fluxes in the
778 outer Solar System. Icarus 264, 369–386.

779 Press, W. H., Flannery, B. P., Teukolsky, S. A., Vetterling, W. T., 1992.
780 Numerical Recipes, 2nd Edition. Cambridge Univ. Press, Cambridge UK.

781 Rosenqvist, J., Lellouch, E., Romani, P. N., Paubert, G., Encrenaz, T., 1992.
782 Millimeter-wave observations of Saturn, Uranus, and Neptune - CO and
783 HCN on Neptune. Astrophys. J. 392, L99–L102.

784 Simonelli, D. P., Reynolds, R. T., 1989. The interiors of Pluto and Charon
785 - Structure, composition, and implications. Geophys. Res. Lett. 16, 1209–
786 1212.

787 Swinyard, B. M., Ade, P., Baluteau, J.-P., Aussel, H., Barlow, M. J., Bendo,
788 G. J., Benielli, D., Bock, J., Brisbin, D., Conley, A., Conversi, L., Dowell,
789 A., Dowell, D., Ferlet, M., Fulton, T., Glenn, J., Glauser, A., Griffin, D.,
790 Griffin, M., Guest, S., Imhof, P., Isaak, K., Jones, S., King, K., Leeks, S.,
791 Levenson, L., Lim, T. L., Lu, N., Makiwa, G., Naylor, D., Nguyen, H.,
792 Oliver, S., Panuzzo, P., Papageorgiou, A., Pearson, C., Pohlen, M., Pole-
793 hampton, E., Pouliquen, D., Rigopoulou, D., Ronayette, S., Roussel, H.,

794 Rykala, A., Savini, G., Schulz, B., Schwartz, A., Shupe, D., Sibthorpe, B.,
795 Sidher, S., Smith, A. J., Spencer, L., Trichas, M., Triou, H., Valtchanov,
796 I., Wesson, R., Woodcraft, A., Xu, C. K., Zemcov, M., Zhang, L., 2010.
797 In-flight calibration of the Herschel-SPIRE instrument. Astron. Astrophys.
798 518, L4.

799 Swinyard, B. M., Polehampton, E. T., Hopwood, R., Valtchanov, I., Lu, N.,
800 Fulton, T., Benielli, D., Imhof, P., Marchili, N., Baluteau, J.-P., Bendo,
801 G. J., Ferlet, M., Griffin, M. J., Lim, T. L., Makiwa, G., Naylor, D. A.,
802 Orton, G. S., Papageorgiou, A., Pearson, C. P., Schulz, B., Sidher, S. D.,
803 Spencer, L. D., van der Wiel, M. H. D., Wu, R., 2014. Calibration of the
804 Herschel SPIRE Fourier Transform Spectrometer. Mon. Not. R. Astron.
805 Soc. 440, 3658–3674.

806 Teanby, N. A., 2007. Constrained smoothing of noisy data using splines in
807 tension. Math. Geol. 39, 419–434.

808 Teanby, N. A., Irwin, P. G. J., 2013. An External Origin for Carbon Monoxide
809 on Uranus from Herschel/SPIRE? Astrophys. J. 775, L49.

810 Teanby, N. A., Irwin, P. G. J., Nixon, C. A., Courtin, R., Swinyard, B. M.,
811 Moreno, R., Lellouch, E., Rengel, M., Hartogh, P., 2013. Constraints on Ti-
812 tan's middle atmosphere ammonia abundance from Herschel/SPIRE sub-
813 millimetre spectra. Plan. & Space Sci. 75, 136–147.

814 Venot, O., Hébrard, E., Agúndez, M., Dobrijevic, M., Selsis, F., Hersant, F.,
815 Iro, N., Bounaceur, R., 2012. A chemical model for the atmosphere of hot
816 Jupiters. Astron. Astrophys. 546, A43.

817 Visscher, C., Moses, J. I., Saslow, S. A., 2010. The deep water abundance
818 on Jupiter: New constraints from thermochemical kinetics and diffusion
819 modeling. Icarus 209, 602–615.

820 Visscher, C., Sperier, A. D., Moses, J. I., Keane, T. C., 2009. Phosphine
821 and Ammonia Photochemistry in Jupiter's Troposphere. In: Lunar and
822 Planetary Science Conference. Vol. 40 of Lunar and Planetary Science
823 Conference. p. 1201.

824 Yung, Y. L., Allen, M., Pinto, J. P., 1984. Photochemistry of the atmosphere
825 of Titan - Comparison between model and observations. Astrophys. J.
826 Supp. 55, 465–506.

Study	Telescope	Freq.	Wavenumber	Uniform†	Step‡		
					v_1	v_2	p_1
		(GHz)	(cm^{-1})	(ppm)	(ppm)	(ppm)	(bar)
Luszcz-Cook and de Pater (2013)	CARMA	115.271	3.845	-	0–0.3	0.93–1.9	0.0025–0.2
	CARMA	230.538	7.670	-	”	”	”
	CARMA	345.796	11.535	-	”	”	”
Lellouch et al. (2010)	Herschel/PACS	∼1750	∼60	-	∼0.5	∼1	∼0.01
Hesman et al. (2007)	JCMT	345.796	11.535	-	0.6±0.4	$2.2^{+0.6}_{-0.4}$	0.006
Lellouch et al. (2005)	IRAM	230.538	7.670	-	0.5±0.1	1±0.2	0.02
Marten et al. (2005)	IRAM	230.538	7.670	1.0±0.2	-	-	-
	JCMT	345.796	11.535	”	-	-	-
	JCMT	461.040	15.379	”	-	-	-
Naylor et al. (1994)	JCMT	230.538	7.670	1.0±0.3	-	-	-
Guilloteau et al. (1993)	IRAM	115.271	3.845	0.6–1.5	-	-	-
Marten et al. (1993)	CSO	230.538	7.670	1.2±0.4	-	-	-
	JCMT	345.796	11.535	”	-	-	-
Rosenqvist et al. (1992)	IRAM	230.538	7.670	0.65±0.35	-	-	-

Table 1: Summary of previous microwave and far-IR CO studies. † Early studies used a profile with a uniform mixing ratio throughout the troposphere and stratosphere. ‡ Recent studies assume a step-type profile defined by a transition pressure p_1, a high pressure uniform abundance v_1, and a low pressure uniform abundance v_2.

Obs. ID	Start Time (UT)	Integration Time (s)	RA (°)	DEC (°)	Dist. (AU)	Disc (")
1342187090	2009-11-19 05:52:45.0	823.0	326.06	-14.06	30.07	2.27
1342187883	2009-12-09 00:26:43.0	823.0	326.34	-13.97	30.40	2.25
1342187884	2009-12-09 00:40:54.0	823.0	326.31	-13.98	30.40	2.25
1342187887	2009-12-09 01:23:18.0	876.0	326.32	-13.97	30.40	2.25
1342195348	2010-04-21 19:57:15.0	1145.0	330.47	-12.53	30.46	2.24
1342195771	2010-05-03 19:03:43.0	1145.0	330.68	-12.46	30.27	2.26
1342196617	2010-05-17 04:43:33.0	1145.0	330.83	-12.42	30.05	2.27
1342197362	2010-05-31 11:27:26.0	1145.0	330.90	-12.41	29.80	2.29
1342197363	2010-05-31 11:46:49.0	1145.0	330.88	-12.42	29.80	2.29
1342197364	2010-05-31 12:06:10.0	1145.0	330.89	-12.42	29.80	2.29
1342197365	2010-05-31 12:25:33.0	1145.0	330.90	-12.39	29.80	2.29
1342197366	2010-05-31 12:44:56.0	1145.0	330.87	-12.40	29.80	2.29
1342197367	2010-05-31 13:04:17.0	1145.0	330.88	-12.39	29.80	2.29
1342197368	2010-05-31 13:23:38.0	3597.0	330.89	-12.40	29.80	2.29
1342198429	2010-06-09 19:52:13.0	13762.0	330.87	-12.42	29.65	2.30
1342208385	2010-11-08 00:51:49.0	839.0	328.16	-13.40	29.82	2.29
1342210841	2010-12-05 15:26:40.0	839.0	328.39	-13.32	30.29	2.25
Total		32687.0				

Table 2: Summary of SPIRE observations extracted from the Herschel Science Archive (`http://archives.esac.esa.int/hsa/whsa/`). RA, right ascension; DEC, declination; Dist., distance between Neptune and Herschel; and Disc, projected diameter of Neptune on the sky.

Temperature profile	CO profile type	Pressure		VMR		χ^2/N
		p_1 (bar)	p_2 (bar)	v_1 (ppm)	v_2 (ppm)	
Cold	Step	0.14	——	0.21	0.80	0.69
Cold	Gradient	0.74	0.0009	0.23	0.91	0.74
Cold	External gradient	0.48	0.0018	0.35	0.93	0.79
Nominal	**Step**	**0.11**	——	**0.22**	**1.03**	**0.63**
Nominal	Gradient	0.75	0.0013	0.23	1.19	0.67
Nominal	External gradient	0.48	0.0035	0.36	1.01	0.89
Hot	Step	0.10	——	0.24	1.41	0.86
Hot	Gradient	0.54	0.0023	0.24	1.55	0.89
Hot	External gradient	0.47	0.0073	0.39	1.52	1.21

Table 3: Retrieved CO profile parameters assuming the nominal, hot, and cold temperature profiles in Figure 2. The external gradient profile has zero abundance for pressures greater than p_1. χ^2/N is the reduced χ^2 misfit and should be $\sim$1 for a model fitting the data to within error – all profiles except the hot external gradient profile provide adequate fits to the data. The nominal temperature profile with a step CO abundance profile (shown in bold) provides the best fit to the observations (Figure 5 and 6).

Temperature profile	Optimal spectrometer	PH_3 band centre (cm^{-1})	Pressure sensitivity (bar)	3-σ UL (ppb)	3-σ UL (x solar P/H†)
Cold	SLW	17.81	0.8–1.2	<5.52	$<1.13\times10^{-2}$
Nominal	SSW	44.46	0.4–0.8	<1.10	$<2.25\times10^{-3}$
Hot	SSW	44.46	0.1–0.7	<0.192	$<3.93\times10^{-4}$

Table 4: PH_3 3-σ upper limits for the three temperature profiles. In each case the optimal spectrometer is the one giving the lowest upper limit. Pressure sensitivity is the full-width half-maximum of the contribution functions shown in Figure 4 and in the absence of photochemistry is determined by the saturation vapour pressure curve. † Equivalent enrichment relative to solar P/H using the abundances from Lodders (2010), i.e. solar P/H=0.281×10^{-6}, implying a solar composition volume mixing ratio $PH_3/(H_2+He)=0.489\times10^{-6}$ (assuming that $He/H_2=0.15$ and all phosphorous is the form of PH_3).

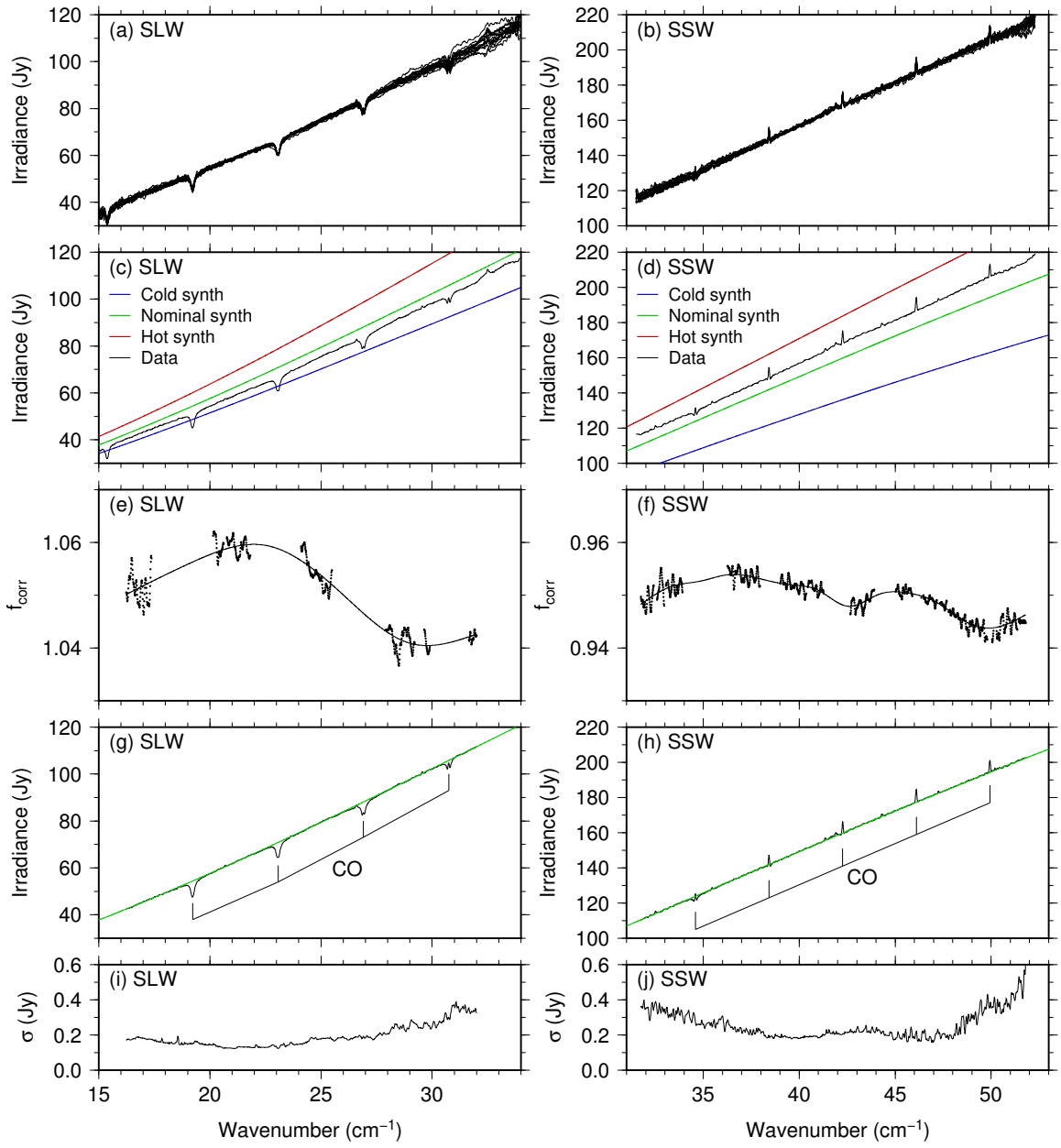

Figure 1: Neptune SPIRE SLW and SSW spectra. (a,b) Individual spectra from the 17 observations in Table 2. (c,d) Weighted mean spectra compared with synthetic baseline spectra (no CO or PH_3) for nominal, hot, and cold temperature profiles. (e,f) Ratio of synthetic spectra to observation in continuum regions for nominal temperature case. The smooth cubic b-spline curve is used to correct the observation for large scale continuum ripples. (g,h) Corrected spectrum for nominal temperature case and (i,j) standard error uncertainties. CO features are clearly visible in the data (labelled).

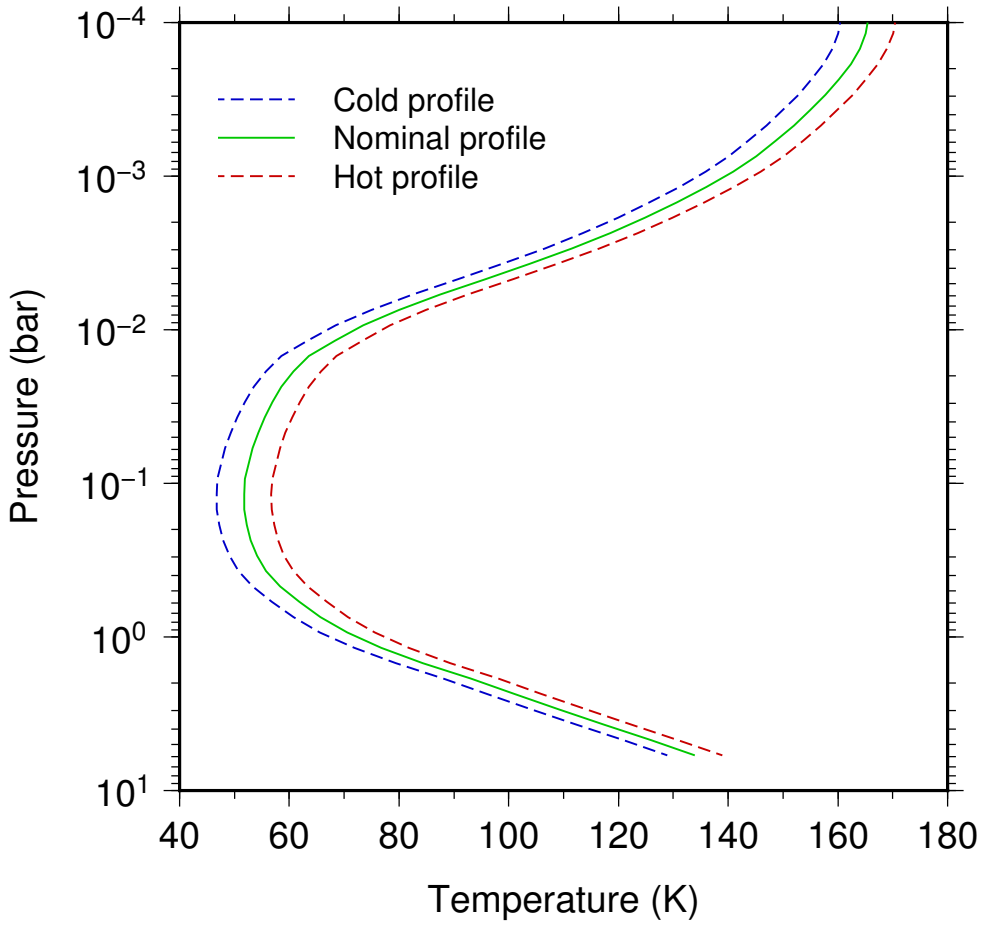

Figure 2: Neptune temperature profiles. The hot and cold profiles are ±5 K from the nominal case, which is based on Lindal (1992) and Fletcher et al. (2010). Our analysis is performed using all three profiles to include the current uncertainty in Neptune's temperature structure.

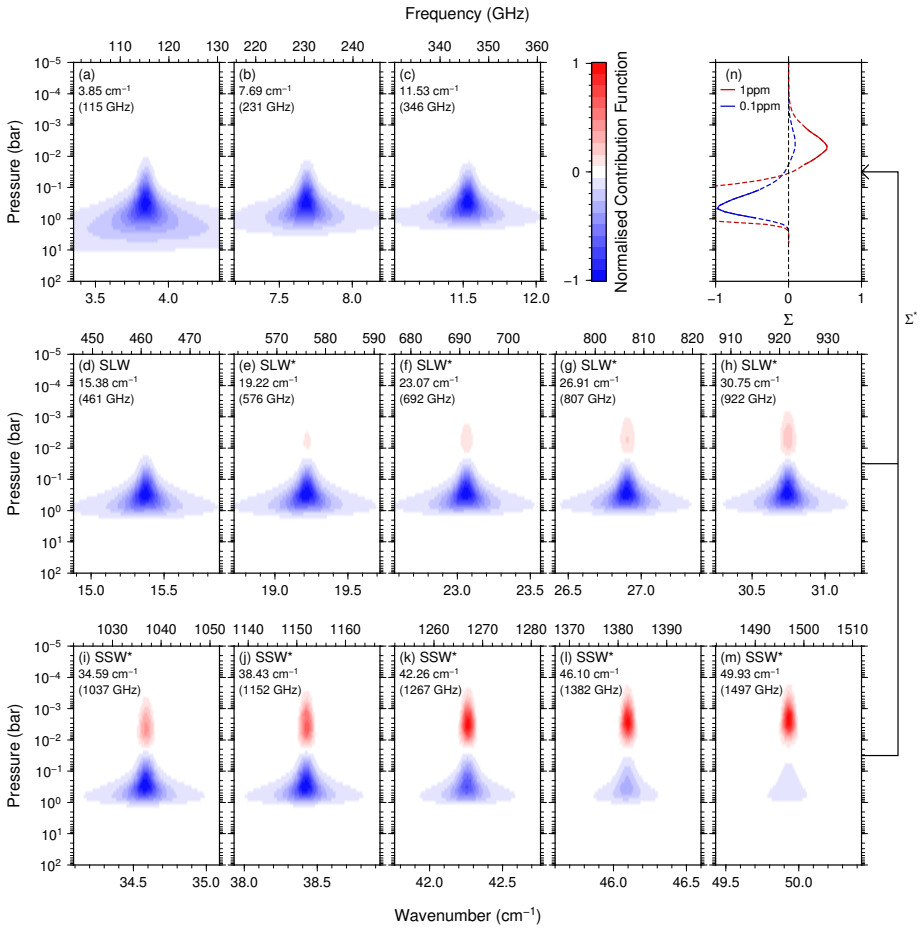

Figure 3: Contribution functions for CO microwave bands. Calculations assume the SPIRE spectral resolution of 0.07373 cm^{-1}, the nominal temperature profile in Figure 2, and 0.1 ppm uniform CO abundance throughout the atmosphere. The upper tropospheric CO abundance gives wide absorption (negative/blue) features that are most prominent at lower frequencies, whereas the stratospheric abundance gives a narrow emission peak (positive/red) that is most prominent at higher frequencies. (a–c) Lowest frequency CO bands studied previously (e.g. by Luszcz-Cook and de Pater, 2013). (d-m) CO bands covered SPIRE, with * indicating the bands analysed here. (n) Total normalised contribution function summed over all analysed wavenumbers in (e–m) for 1 ppm CO (red) and 0.1 ppm CO (blue), appropriate for the stratosphere and troposphere respectively. Solid/dashed line indicates where these abundances are appropriate/not appropriate. Information content is restricted to the 0.001–0.01 and 0.1–1 bar pressure regions for SPIRE. The lower frequency lines (a–c) probe slightly deeper to ∼3 bar, assuming a typical 5–10 GHz bandwidth (Luszcz-Cook and de Pater, 2013). The transition pressure used to define the step profile in previous studies typically falls in the 0.01–0.1 bar region, where there is little sensitivity.

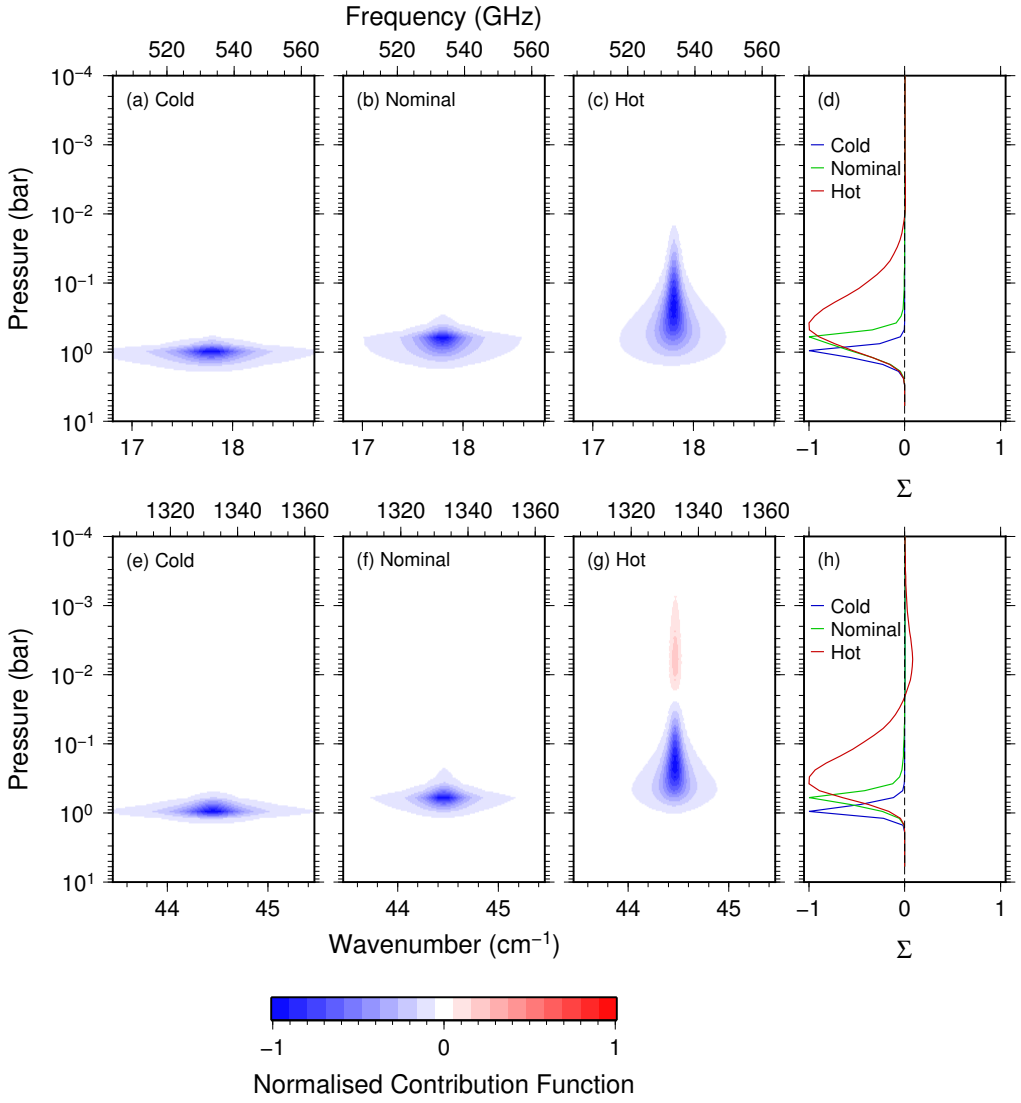

Figure 4: Phosphine contribution functions for the 17.81 cm^{-1} (a–d) and 44.46 cm^{-1} (e–h) features under different temperature profile assumptions. For the nominal and cold cases saturation limits stratospheric abundances to negligible amounts. For the hot case some PH_3 can enter the stratosphere giving a small emission feature. (d,h) Total normalised contribution function summed over all wavenumbers in each band. Information is limited to the upper troposphere (0.1–1.2 bar).

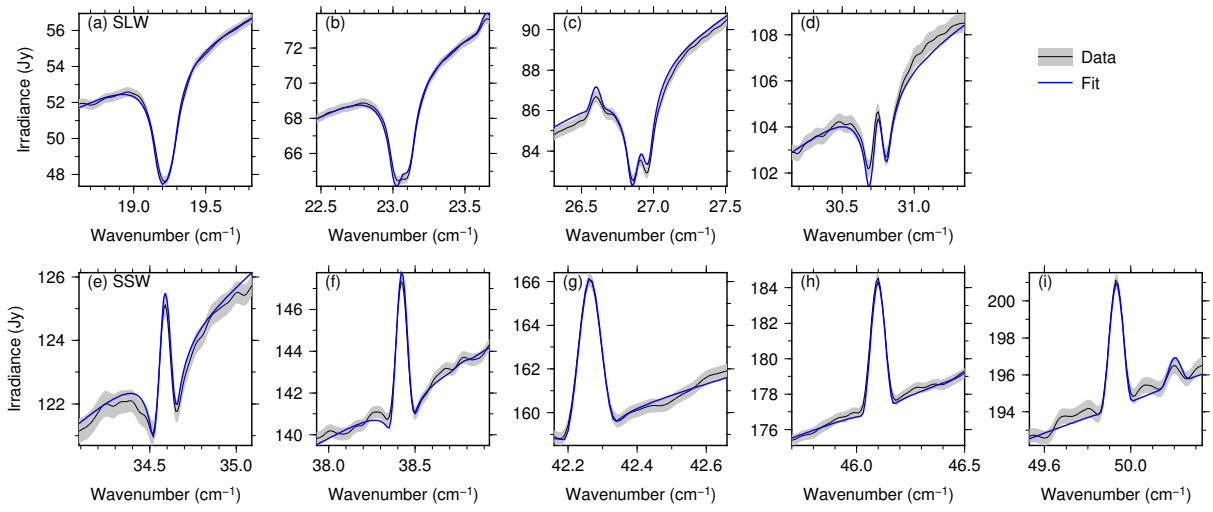

Figure 5: Fitted CO features using the nominal temperature profile and a step VMR profile (bold profile highlighted in Table 3, and plotted in Figure 6). All nine CO bands are well fitted. The other profiles in Table 3 provide comparable fit qualities.

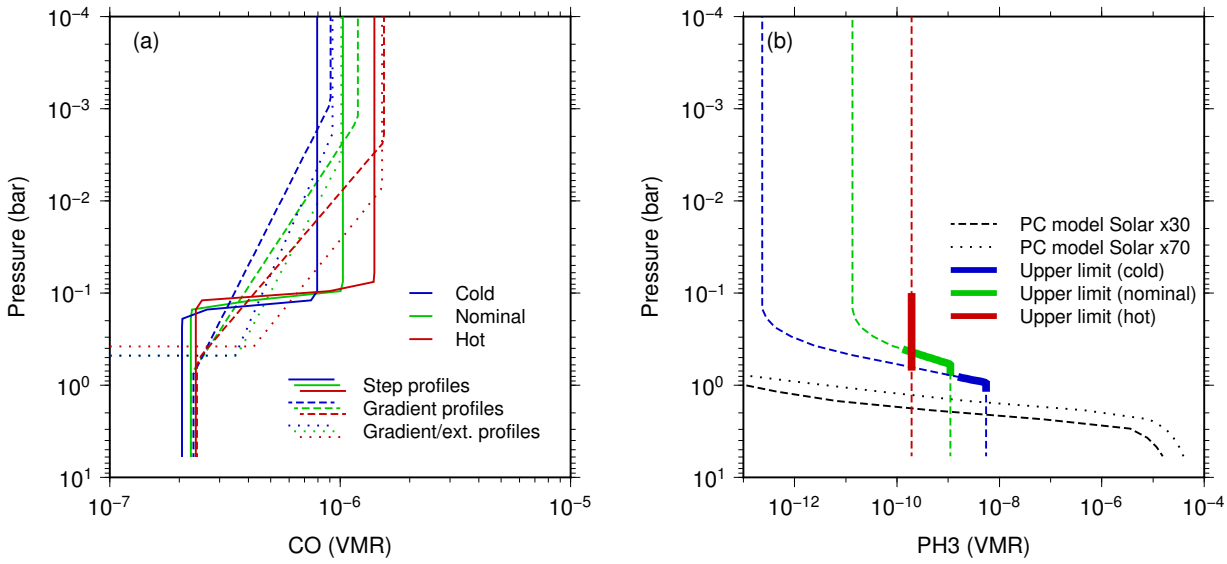

Figure 6: Fitted CO VMR profiles and PH_3 upper limits. (a) CO profiles have 0.80–1.55 ppm in the stratosphere and 0.21–0.39 ppm in the upper troposphere. These data do not require significant deep CO abundance. (b) Phosphine upper limits are consistent with our simple photochemical model profiles, which predict significant PH_3 removal by photolysis for pressures less than ∼2 bar. Upper limit profiles are limited by condensation, which occurs at pressures less than ∼1 bar. Note that the hot profiles require more stratospheric CO due to the rescaling of the continuum, which increases the contrast of the emission peak (the opposite is true for the cold profile).

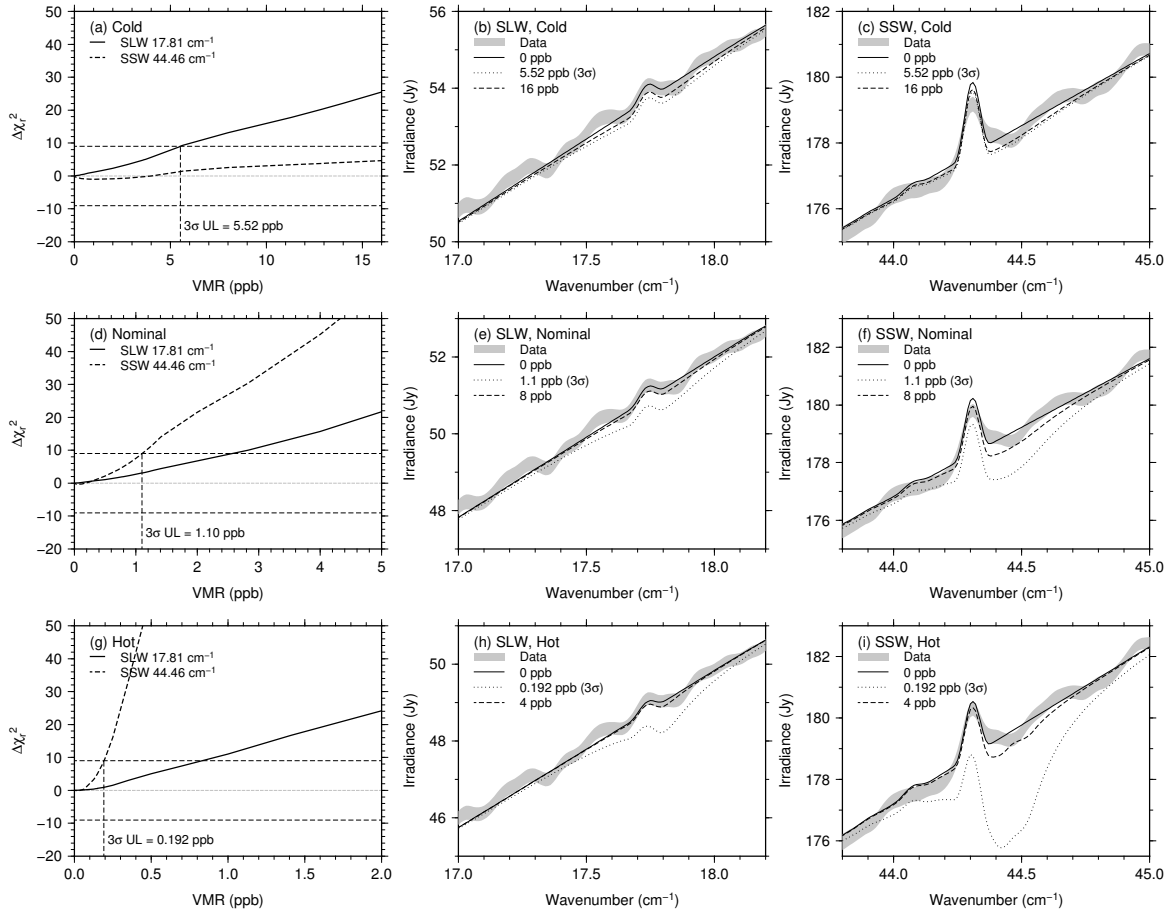

Figure 7: Phosphine upper limits. (a,d,g) variation of χ^2 as a function of deep phosphine abundance for the two spectral bands and all three temperature profiles. No significant PH_3 is detected and upper limits of 0.192–5.52 ppb are inferred. Observations and synthetics with zero PH_3 abundance, 3-σ PH_3 abundance, and an enhanced abundance to show the PH_3 feature shape more clearly are shown in (b,c) for the cold profile, (e,f) for the nominal profile, and (h,j) for the hot profile.